Article

Redox Cycling Driven Transformation of Layered Manganese Oxides to Tunnel Structures

Haesung Jung, Martial Taillefert, Jingying Sun, Qian Wang, Olaf J. Borkiewicz, Pan Liu, Lufeng Yang, Shuo Chen, Hailong Chen,* and Yuanzhi Tang*

Read Online

ACCESS | 📊 Metrics & More | 📰 Article Recommendations | 🆂🅸 Supporting Information

ABSTRACT: Mn oxides are among the most ubiquitous minerals on Earth and play critical roles in numerous elemental cycles in biotic/abiotic loops as the key redox center. Yet, it has long puzzled geochemists why the laboratory synthesis of todorokite, a tunnel-structured Mn oxide, is extremely difficult while it is the dominant form over other tunneled phases in low-temperature natural environments. This study employs a novel electrochemical method to mimic the cyclic redox reactions occurring over long geological time scales in an accelerated manner. The results revealed that the kinetics and electron flux of the cyclic redox reaction are key to the layer-to-tunnel structure transformation of Mn oxides, provided new insights for natural biotic and abiotic redox reactions, and explained the dominance of todorokite in nature.
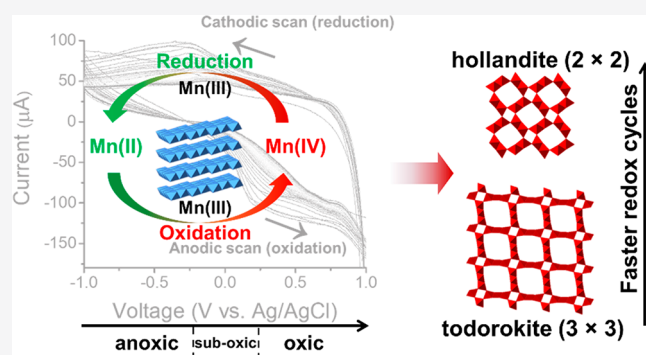
INTRODUCTION

Mn(III,IV) (oxyhydr)oxides (hereafter Mn oxides) are a group of minerals that exist ubiquitously in terrestrial and aquatic environments. They are among the most reactive minerals in nature and mediate the fate and transport of numerous contaminants and nutrients via adsorption, coprecipitation, and redox reactions. They are also highly impactful in the evolution of biotic systems on Earth over geological time scales, as their formation and structure dictate the bioavailability of the critical micronutrient Mn, an important constitute or activator of multiple enzymes for a number of physiologic processes such as photosynthesis.[1] As one of the most powerful groups of natural oxidants, Mn oxides contribute significantly to the oxidation of recalcitrant organic carbon, such as the degradation of lignin/litter to bioavailable substrates that feed into the microbial food web.[2] They also play key roles in a range of critical redox processes such as microbial respiration and photochemical reactions and significantly impact the flow of electrons and energy in natural systems,[3−6] functioning as Nature's Battery.

In natural systems, the formation of Mn oxide solid phases commonly starts with the oxidation of Mn(II) species (e.g., dissolved $Mn^{2+}(aq)$ through a range of biotic and abiotic processes, such as those catalyzed by microbial enzymatic activities, reactive oxygen species, and mineral surfaces.[3,7−10] The newly formed oxides typically occur as poorly crystalline, highly disordered, and highly reactive layered phases that are structurally similar to δ-MnO_2 (vernadite) or birnessite.[10]

These fresh oxides can subsequently undergo diagenesis and transformation at oxic−anoxic interfaces such as those in ocean sediments, which can induce a gradient of reduction potential within a few centimeters in the sediments and result in continuous redox cycles between Mn(II) and Mn(IV).[6,11,12] Through complex biogeochemical processes such as precipitation, dissolution, ripening, and transformation, natural Mn oxides occur in more than 30 species in current environments and are commonly classified as layer (i.e., phyllomanganates) and tunnel structures (i.e., tectomanganates).[13]

Although both composed of MnO_6 octahedra as the main building blocks, layer- and tunnel-structured Mn oxides exhibit distinctively different redox, sorption, electrochemical, and photochemical reactivities.[14,15] Such differences can give rise to large uncertainties in geochemical models involving Mn oxides as critical components, as demonstrated in several newly emerged powerful paleoproxy systems (e.g., the Cr, Mo, and Tl isotope systems) for tracing Earth's oxygen evolution history.[16−20] Although extensive research efforts have improved our understanding of biotic/abiotic formation mechanisms of layered Mn oxides in the past decades[8,21] and some recent studies are providing new insights on the
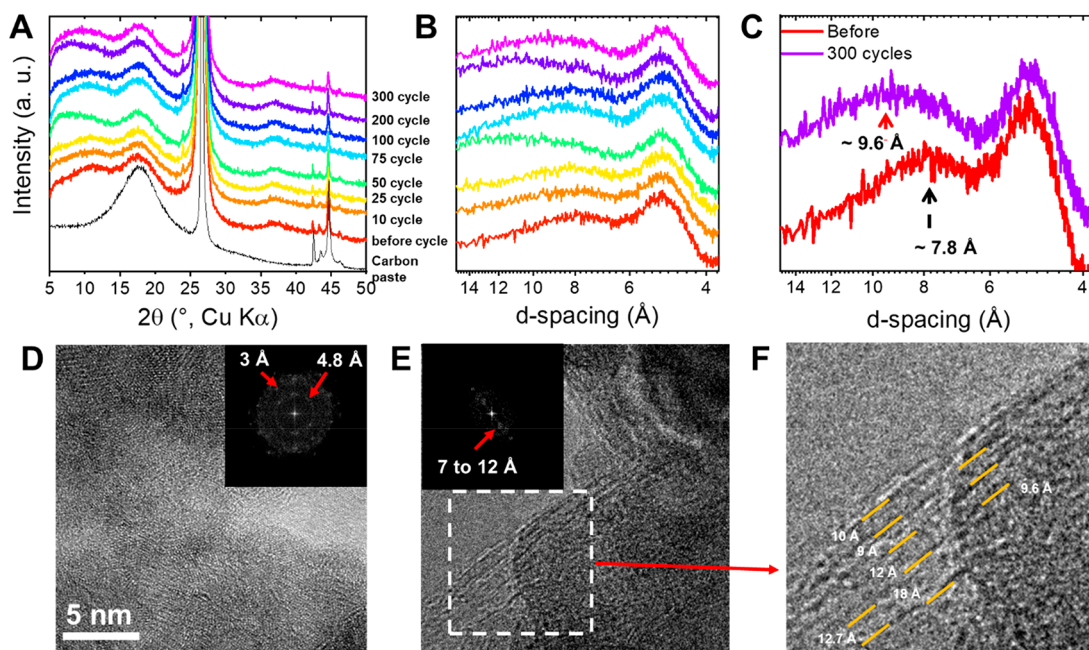
Figure 1. Transformation of δ-MnO$_2$ nanosheets to tunnel-structured todorokite driven by repeated redox cycling. (A and B) From bottom to top, XRD patterns of carbon paste, unreacted δ-MnO$_2$ (0 cycle), and δ-MnO$_2$ after 10−300 cycles at 100 mV/s. (C) Shift of the δ-MnO$_2$ (001) basal plane diffraction peak to the (100, 001) peak of todorokite after 300 redox cycles. (D−F) HRTEM images and fast Fourier transform of selected areas showing atomic distances, ranging from ~9 to 18 Å, occurring from the direction perpendicular to tunnels, typical of todorokite after 300 cycles.

formation mechanism and structure of todorokite in synthetic/engineered systems,[22−24] the formation, pathway, and kinetics of tunneled Mn oxides in natural biogeochemical systems still remain elusive.[13,25] Besides layer-structured birnessite, tunnel-structured todorokite (3×3 tunnel size) is the other most commonly observed phase in natural systems.[26] Yet, laboratory efforts attempting to produce todorokite under low-temperature circumneutral environmental conditions have been surprisingly difficult. To date, it appears that laboratory syntheses of todorokite from layered Mn oxides require pH values far deviating from natural circumneutral conditions and/or elevated, nonambient temperatures (e.g., those under hydrothermal or reflux settings).[25,27,28] Such observations are significantly inconsistent with the dominant presence of todorokite in natural low-temperature environments, which presents a puzzling mystery for geoscientists. Moreover, the phase selection mechanism(s)/pathway(s) during layer to tunnel structure transformation is even less explored and is elusive as well. The predominant occurrence of todorokite in natural environments over other tunnel-structured Mn oxides, such as pyrolusite (β-MnO$_2$, 1×1 tunnel size), is also not supported by thermodynamics, as pyrolusite (not todorokite) is the most thermodynamically stable Mn(VI) oxide with a formation energy of −465.1 kJ/mol.[29,30]

Recent studies suggested the important roles of Mn(II) adsorption and interlayer Mn(III) for the transformation from layer-structured δ-MnO$_2$ to tunnel-structured Mn oxides.[24,25] These studies, though still conducted under pH or temperature conditions deviating from low-temperature circumneutral conditions, motivated us to investigate the roles of Mn(III) supplies in natural environments in inducing the layer-to-tunnel phase transformation. It should be noted that many natural geochemical reactions more commonly do not occur in one pot and finish in one run as in designated laboratory syntheses. The varying sometimes cyclic fluctuations of elemental concentration and electron flux in natural environments (e.g., those caused by day−night cycles, tidal cycles, oxic−anoxic interfaces, and microbially induced microenvironments, etc.) means that reaction kinetics can play very important roles in addition to the thermodynamic driving forces. We hypothesize that redox fluctuation (such as those commonly observed at natural oxic−anoxic interfaces) is a key driving factor for the layer-to-tunnel phase transformation of Mn oxides in nature. Such transformation overall involves the formation of Mn oxides, biotic/abiotic reduction of Mn oxides, production and adsorption of dissolved Mn^{2+}(aq), and formation of interlayer Mn(III) under the fluctuated redox environments. Investigation of such redox fluctuating/cyclic processes is very challenging as they may spread over very long geological time scales. Here we report our novel approach of using an electrochemical method to mimic and simulate such processes in an accelerated manner and to testify our hypothesis. The phase transformation mechanism of δ-MnO$_2$ (the most common structural analog for the freshly precipitated layered Mn oxides) was investigated using cyclic voltammetry (CV), which can mimic repeated redox cycles such as those occurring at the oxic−anoxic interfaces in natural systems (e.g., sediments)[6,12] as well as complementary structural characterization. The results reveal that repeated redox cycling indeed is key for triggering δ-MnO$_2$ transformation to tunneled Mn oxides (e.g., todorokite) at room temperature and circumneutral pH conditions. Further analyses also elucidated the factors controlling the phase selection among different tunnel-structured Mn oxides in natural settings.
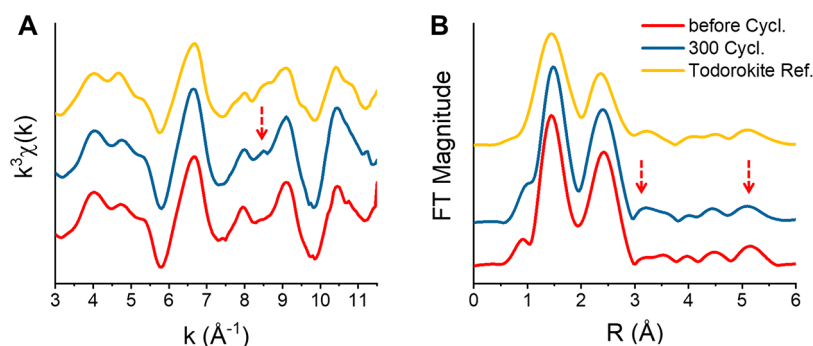
Figure 2. EXAFS analysis of δ-MnO_2 reaction products. (A) Mn K-edge EXAFS spectra and (B) Fourier transform of δ-MnO_2 before and after 300 cycles compared to a todorokite reference compound.

■ RESULTS AND DISCUSSION

Redox Cycling-Induced Phase Transformation from δ-MnO_2 to Todorokite. Cyclic voltammetry (CV) as a popular electrochemical method is widely used to investigate redox reactions. It can be used as a good simulator for the fluctuating/cyclic long-time-scale geochemical reactions, where the reactions can be reasonably accelerated with facile controlled current density and voltage scanning rate. In this study, the investigation on Mn oxide formation was conducted with CV scanning on a δ-MnO_2 electrode/Pt electrochemical cell between −1 and 1 V (vs Ag/AgCl reference electrode). This voltage range simulates natural redox interfaces such as the oxic−anoxic interface within ocean sediments and enables the redox cycling of δ-MnO_2.[31] Upon continuous redox cycling we observed the transformation from layer-structured δ-MnO_2 to tunnel-structured phase as revealed by X-ray diffraction (XRD) (Figure 1). Despite the strong diffraction peaks from graphite in the carbon paste (as conductive additive) in the δ-MnO_2 electrode, low-intensity and broad diffraction peaks of δ-MnO_2 at ~11.2° and 37° 2θ can be clearly observed, consistent with its poorly crystalline nature and the few-layer stacking structure (4−6 layers) (Figure 1A).[32] After 300 redox cycles at 100 mV/s rate, no noticeable shifts in the *hk* bands at 37° of δ-MnO_2 were observed but a shift of the (001) basal plane of δ-MnO_2 from ~11.2° to ~8−9° 2θ (Figure 1A) was observed, corresponding to a change in *d* spacing from ~7.8 to ~9−12 Å (Figure 1B and 1C). With increasing number of cycles, this peak showed dynamic changes in its width and position between ~8.5 and 12 Å (Figure 1B), suggesting a dynamic change in the mineral structure. Among more than 30 species of naturally occurring Mn oxides,[13] the observed diffraction peak at ~7.5−9.5° 2θ only occurs in buserite and todorokite. Buserite is an unstable hydrated form of layer-structured birnessite, and its structure readily collapses to birnessite upon dehydration in a desiccator or vacuum.[33] As our samples were freeze dried before XRD measurements, the formation of buserite can be ruled out. Therefore, todorokite, which ideally has a 3 × 3 tunnel structure but can also occur in varied tunnel sizes such as 3 × 2 (7.3 Å), 3 × 4 (12.3 Å), 3 × 5 (14.6 Å), etc.,[26,34,35] represents the only possible phase that explains the observed diffraction peak. The formation of todorokite was also confirmed by synchrotron XRD (SXRD) analyses (Figure S1). With increasing numbers of redox cycles, both in situ (Figure S1A) and ex situ SXRD (Figure S1B and S1C) showed emerging diffraction peaks from todorokite at ~9−12 Å. Even though all samples display a hump at ~18° (from the mineral oil in carbon paste), the redox-cycled

samples show a slight shift in the diffraction angle, making the peak asymmetric. The asymmetric peak is obvious for the 300-cycled sample (Figure S1B).

To clearly confirm the formation of poorly crystalline todorokite through redox cycles, the formation of todorokite was further confirmed by fast Fourier transform (FFT) of high-resolution transmission electron microscopy (HRTEM) images (Figure 1D). Consistent with the better crystallinity after 300 redox cycles as compared to the pristine δ-MnO_2 (Figures 1D and S2), FFT showed distinctive diffraction rings at 4.8 and 3 Å *d* spacing, which were not observed in the FFT of pristine δ-MnO_2 (Figure S2A).[27,28,34] While the poorly crystalline nature of the samples (as shown in in situ/ex situ XRD analyses) and the presence of carbon paste made it very difficult to obtain atomic resolution HRTEM images such as those in recent studies on synthetic todorokite,[24,36] our HRTEM and FFT analyses showed poorly crystalline todorokite at the direction perpendicular to the tunnels and associated diffuse scattering rings at around 7−12 Å *d* spacing (Figure 1E and 1F). Thus, XRD and HRTEM both point to the transformation of δ-MnO_2 to todorokite upon repeated redox cycling. To the best of our knowledge, this is the first time that the transformation of layered Mn oxide phases (e.g., δ-MnO_2) to todorokite under low-temperature and circumneutral pH conditions is achieved in laboratory settings.

While structural changes occurred during redox cycling, no significant change was observed in the average oxidation state of the solid phases. During the 300 redox cycles, Mn(IV) was the most dominant oxidation state as revealed by Mn K-edge X-ray absorption near-edge structure (XANES) spectroscopy and related linear combination fitting (LCF) results (Figure S3 and Table S1). LCF only showed a slight fluctuation of the average oxidation state between 3.72 and 3.76 during redox cycles. Compared to pristine δ-MnO_2, 300 redox cycles led to an increase in Mn(III) fraction from 15.4 to 17.2%, as well as a decrease in Mn(II) fraction from 5.7% to 4.7%. Mn K-edge extended X-ray absorption fine structure (EXAFS) spectra showed substantial changes in local structure from redox cycling (Figure 2A and Table S2). The change primarily occurred at 7.5−9.5 Å^{-1} in *k* space, the well-known "indicator region" for phyllo- and tectomanganate structures.[33,37−39] δ-MnO_2 and birnessite with hexagonal symmetry typically show sharp peaks at 8−9.2 Å^{-1}. While these peaks can also occur for tunnel-structured Mn oxides at lower intensity, due to another peak at 8.5 Å^{-1}, this indicator region would also show a steady rising slope.[33,39] The EXAFS spectrum of the reaction product after 300 cycles showed the emergence of the 8.5 Å^{-1} peak and accompanied decrease in height for the peaks in the 8−9.2 Å^{-1}

region, resembling the spectra of todorokite. Such trend was also reflected in the corresponding Fourier transforms of EXAFS spectra (Figure 2B). As compared to pristine δ-MnO$_2$, the peak increase of the cycled sample at 3.2 Å in R space is characteristic of tunnel-structured Mn oxides.[25] In addition, Mn–Mn multiple scattering at 5.2 Å is weaker than that of δ-MnO$_2$ due to the collapse of the layered structure.[40]

Taken together, XRD, HRTEM, and EXAFS results demonstrate the transformation of δ-MnO$_2$ to todorokite. The redox-cycled sample, however, still contain a significant amount of δ-MnO$_2$ along with todorokite. XRD and FFT of the redox-cycled sample show amorphous-like diffraction at 2.4 Å, occurring from the *hk* band (20, 11) of δ-MnO$_2$ as shown in XRD and FFT in the pristine sample of δ-MnO$_2$ (Figures 1A and S2A). In EXAFS and its Fourier-transformed spectra, the redox-cycled sample also showed less significant features of todorokite compared to well-crystalline todorokite samples (Figure 2). The presence of residual δ-MnO$_2$ is possibly due to the incomplete transformation caused by kinetics constraints or experimental set up and warrants further investigation on the influencing factors on the degree of transformation and crystallinity of todorokite products. Previous studies on the transformation of birnessite to todorokite used hydrothermal or reflux setups, which are homogeneous reactions induced through thermal energy.[27,28] The mineral transformation in our study proceeded via interfacial electron transfer, which likely only occurred at or near the δ-MnO$_2$ particle surface. The co-occurrence of phyllomanganate (e.g., birnessite) and todorokite has been evidenced in a variety of naturally occurring Mn oxides such as Mn nodules and desert varnishes. It is plausible that natural redox reactions, which occur as interfacial processes through electron transfers between microbes, minerals, organics, and metals,[35] are at least partially responsible for such co-occurrence.

Electron Transfer Mechanism. After successfully obtaining todorokite in ambient environment, the outstanding question is why it only forms in such cyclic redox reactions but not in previous "one-pot" reactions. To decipher this question we explored the electron transfer mechanism between dissolved Mn^{2+}(aq) and Mn(IV) via another set of CV measurements (Text S3, Figure 3). Instead of the δ-MnO$_2$ and

carbon paste mixture used for previous experiments, in this set of experiments only carbon paste was used as the working electrode with 100 μM dissolved Mn^{2+}(aq) (a representative concentration in ocean sediment pore water[6]) in the reaction solution. This experiment is designed to assign the redox peaks observed in previous δ-MnO$_2$ voltammograms (Figure S4), and the results revealed that the transformation between Mn(II) and Mn(IV) is through an overall two-step, one-electron transfer mechanism and that Mn(III) formed during the cyclic redox reactions plays a key role, elaborated as follows.

To avoid the formation of Mn oxides before cycling, which typically occurs anodically at 0.8 V in the presence of dissolved Mn^{2+}(aq) at pH 7 (Figure S4), the voltage was swept from −1 to 1 V (anodic scan) and then returned to −1 V (cathodic scan). During the first cycle only the well-known oxidation peak of dissolved Mn^{2+}(aq) to solid Mn(III/IV)[41] was detected at 0.8 V in the anodic scan (red line in Figure 3). Interestingly, the returning cathodic scan of the first cycle showed two distinctive reduction peaks at −0.05 and 0.6 V (Figure 3). In the second anodic scan, however, a new oxidation peak occurred at 0.43 V. The difference between the first and the second cycles suggest the occurrence of two different redox reactions. The first reaction proceeds between dissolved Mn^{2+}(aq) and solid Mn(III/IV) oxide phase(s). The other reaction takes place between Mn(II) and Mn(IV) in solid Mn oxide phase(s), as evidenced from the oxidation peak produced during the second anodic scan.

The redox peaks produced by the Mn oxide surface also provide crucial information on the electron transfer mechanism during redox cycling (Figure 3). With increasing number of cycles the cathodic peak at −0.05 V shifted slightly to lower voltage and became asymmetric in shape as a result of the emergence of a new cathodic peak at around −0.25 V. Previous studies assigned these two peaks to the two-step reduction of Mn(IV) oxide to Mn(II) oxide.[41] Thus, the first and second peaks at −0.05 and −0.25 V in our cathodic scan likely resulted from the successive reduction of Mn(IV) to Mn(III) and Mn(III) to Mn(II). On the other hand, although the oxidation peak at 0.43 V in the second cycle (navy line in Figure 3) is rarely observed previously, it can be assigned based on the simultaneous evolution of shapes of the reduction and oxidation peaks. With increasing number of cycles, the oxidation peak at 0.2 V became stronger than that when it initially appeared at 0.43 V, while at the same time, the reduction peak initially occurring at −0.05 V gradually shifted to lower voltage with more pronounced asymmetry. On the basis of these corresponding gradual changes of the reduction and oxidation peaks during redox cycles, we infer that the voltammetric peaks at 0.2 and 0.43 V result from the oxidation of Mn(II) to Mn(III) and Mn(III) to Mn(IV), respectively, and that the peaks at −0.05 and −0.25 V are from the reduction of Mn(IV) to Mn(III) and Mn(III) to Mn(II), respectively. We therefore propose that redox cycles promote a two-step, one-electron transfer mechanism between Mn(II) and Mn(IV) in the structure with a solid Mn(III) intermediate (i.e., Mn(IV) → Mn(III) and Mn(III) → Mn(II)), which facilitates formation of the tunnel structure. In addition, it is worth noting that with the CV experiment under different pH conditions electron transfer in solid Mn oxide via H$^+$ participation is excluded (Figure S5).

Roles of Interlayer Mn(III) in the Phase Transformation. We further validate that interlayer Mn(III),
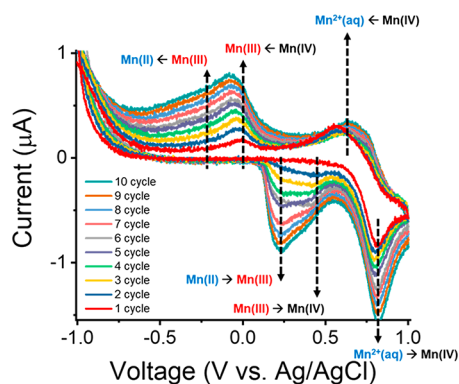
Figure 3. Cyclic voltammetry curves of a 100 μM Mn^{2+} solution cycled 10 times between −1 and 1 V at pH 7. Voltammetric peaks, resulting from redox reactions between Mn(II) and Mn(IV) in solid Mn oxide, changed asymmetrically with increasing numbers of cycles. This result suggests a two-step, one-electron transfer mechanism between structural Mn(II) and structural Mn(IV) with the formation of intermediate Mn(III).
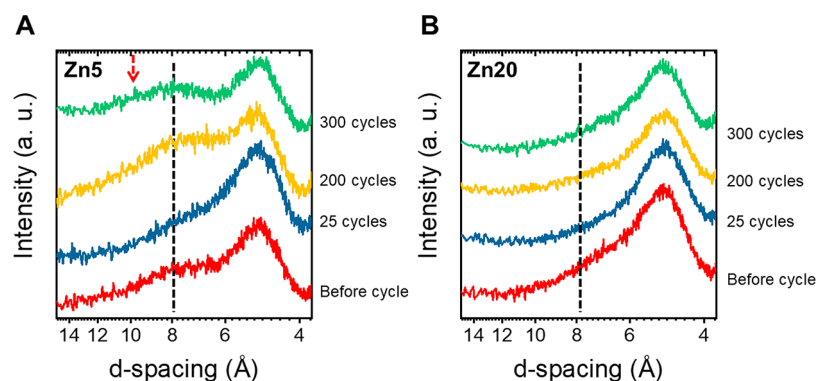
Figure 4. Suppressed transformation of Zn-coprecipitated δ-MnO$_2$ to todorokite. XRD patterns of Zn-coprecipitated δ-MnO$_2$ samples (A) Zn5 and (B) Zn20 before and after 25−300 redox cycles. Black dashed line indicates the d spacing of the (001) basal plane of Zn-coprecipitated δ-MnO$_2$ samples as shown in the broad and weak sample diffraction before cycle. Red arrow points to a diffraction shoulder at $\sim$10 Å after 300 cycles in Zn5 that emerged from the formation of todorokite through redox cycling.
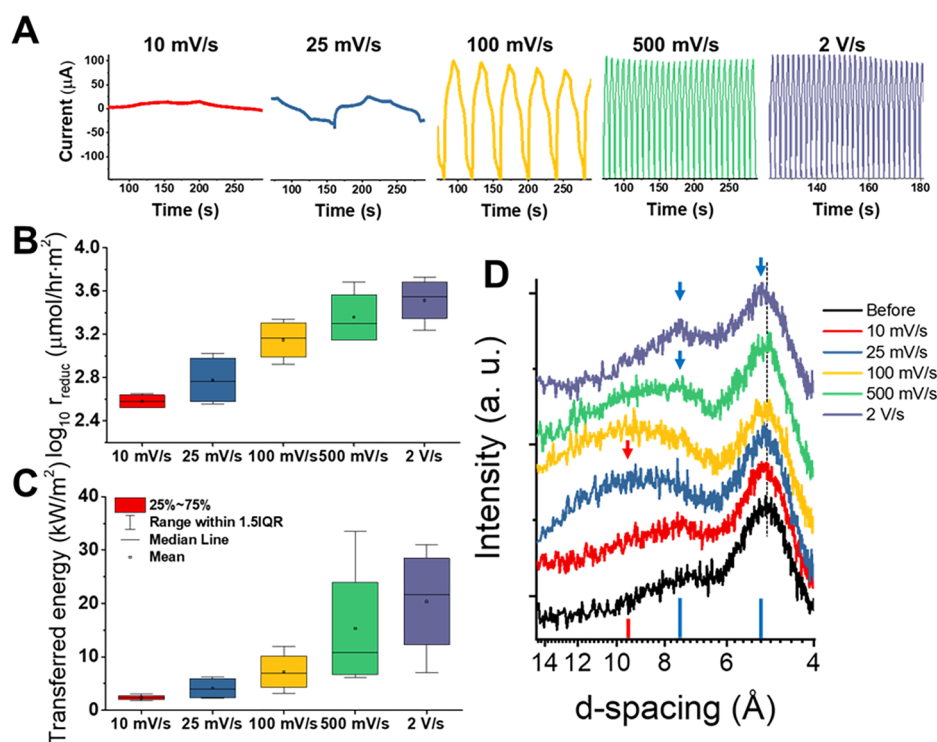
Figure 5. Effect of the frequency and amplitude of repeated redox cycles on the tunnel size of δ-MnO$_2$ transformation products. (A) Current flow as a function of time under varied scan rates. (B) Reduction rates obtained from the varied voltage scan rates. (C) Applied power resulting from electron flux during redox reaction under varied voltage scan rates. Average and error range were obtained by analyzing and averaging CV curves at 10, 100, 200, and 300 redox cycles. (D) XRD showing the change of tunnel size depending on voltage scan rates. Bottom red vertical line represents the (100, 001) diffraction peak of todorokite (3 × 3 tunnel structure). Red arrow indicates the emerged diffraction peak of todorokite. Bottom blue vertical lines indicate the (−101, 10−1) and (200, 002) diffraction peaks of hollandite (2 × 2 tunnel structure). Blue arrows indicate the emerged diffraction peaks of hollandite. Black dashed line is a visual guideline of the change in peak symmetry due to emerged diffraction from hollandite at 2 V/s.

occurring during the reduction from Mn(IV) to Mn(II), is a key factor in inducing the layer-to-tunnel structure transformation. When Mn(III) is produced from the reduction of layer Mn(IV) in δ-MnO$_2$, Mn(III) may migrate to interlayer sites to reduce steric layer strain due to the Jahn−Teller distortion of Mn(III) atoms,[42,43] leaving a vacant site at its original position. Previous studies highlighted the importance of interlayer Mn(III) for the transformation of layered Mn oxide to todorokite, which is based on the condensation of interlayer Mn(III) to form tunnel walls.[24,25,28] To elucidate the role of interlayer Mn(III) in this transformation, we use Zn-

coprecipitated δ-MnO$_2$ samples instead of pure δ-MnO$_2$ as starting material for the electrode. The reason for choosing Zn-coprecipitated δ-MnO$_2$ is because Zn coprecipitation with δ-MnO$_2$ strongly repels interlayer Mn(III) and decreases interlayer Mn(III) content due to the stronger affinity of Zn(II) for interlayer sites compared to Mn(III).[32] We tested two Zn-coprecipitated δ-MnO$_2$ samples named Zn5 and Zn20 based on the Zn:Mn molar ratio during synthesis (details in Text S1 and Table S3). After CV redox cycling, sample Zn5 displayed a broader diffraction at 6−12 Å d spacing, due to the emerging peak at $\sim$10 Å, as compared to Zn5 before cycle

(Figure 4A). Interestingly, no obvious structure change was observed by XRD for sample Zn20 (Figure 4B), which contains ~5 times higher Zn concentration than Zn5 (Table S3). These results demonstrate that the repelling effect of Zn (due to its stronger affinity for interlayer sites than Mn(III)) prevented the migration of Mn(III) (produced from Mn(IV) reduction) into the interlayer sites and the subsequent transformation to todorokite.

Besides the direct generation of Mn(III) via CV-induced redox cycles, comproportionation of Mn^{2+}(aq) and Mn(IV) may represent an alternative source of Mn(III). This reaction may occur if the reduction of structural Mn(IV) releases Mn^{2+}(aq) into the solution, which can subsequently adsorb on δ-MnO_2.[25] However, based on the negligible concentration of dissolved Mn^{2+}(aq) measured in our system (Table S4), such Mn^{2+}(aq)-driven transformation process can be ruled out in our current set up. Thus, taken together, our findings provide further direct evidence that interlayer Mn(III) is critical for the induction of layer-to-tunnel structure transformation of Mn oxides.

Factors Governing Phase Selection and Implications for Natural Systems. Although tunnel-structured Mn(IV) oxides has a number of polymorphs, such as those with 1 × 1 or 2 × 2 tunnel sizes (Figure S7), we only observed the transformation to todorokite (3 × 3 tunnel size) through redox cycles at a scan rate of 100 mV/s between −1 and 1 V. Interestingly, todorokite is not the thermodynamically stable phase of tunnel-structured Mn oxides. This implies that kinetics plays a critical role in phase selection. To further elucidate the impact of kinetics, we conducted CV experiments at different scan rates. Strikingly, with increased scan rate, transformation from δ-MnO_2 to smaller tunnel sized Mn oxide, e.g., hollandite (α-MnO_2; 2 × 2 tunnel) (Figure 5D), was triggered and significantly facilitated. The currents of CV scans at different rates are shown in Figure 5A. The integration of reduction peak area from current vs time and current vs voltage plots are calculated, respectively (Figure S6 and Tables S5 and S6). By taking into account the active surface area of the electrode, the reduction kinetics from Mn(IV) to Mn(II) and the transferred power per active surface area are shown in Figure 5B and 5C, respectively. It appears that a higher scan rate results in faster redox kinetics and greater power per surface area of Mn oxides (also see Tables S5 and S6). Figure 5D shows XRD patterns of the reaction products obtained at different rates; it is clear that the peaks shifted toward lower $d$spacing values with increasing scan rate (Figure 5D). Specifically, when scanned at a 2 V/s rate, new peaks occurred at 7.3 and 5.1 Å with a smaller peak width and higher peak intensity, indicating the formation of 2 × 2 tunnel-structured hollandite, which is also confirmed by HRTEM and FFT analyses (Figure S8). It appears that the higher current flow at faster scan facilitates transformation to smaller tunnel size, which has a higher energy barrier of layer-to-tunnel transition.[22]

This new finding on the kinetics-dependent phase selection prompted us to think about the reaction rates and electron flux of biotic/abiotic oxidation and reduction processes in the nature. In order to compare the reduction rates obtained from the literature (under different experimental conditions) and the rate of electrochemical reduction of δ-MnO_2 in this study, pseudo-first-order rate constants (k_{obs}) are used by dividing the reaction rate by the effective surface area (Figure 6 and Table S7). The rate of δ-MnO_2/birnessite reduction induced by
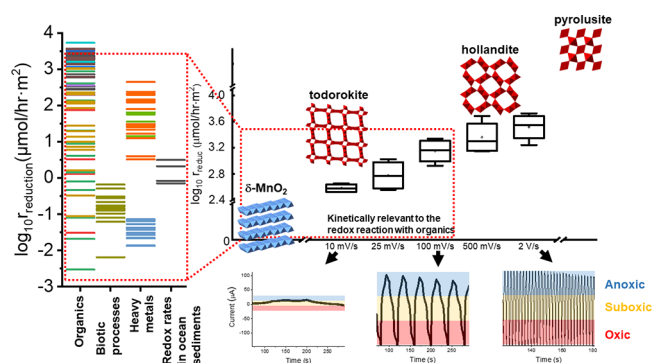
Figure 6. Correlation between the abundance of different tunnel-sized Mn oxides and the environmentally relevant redox kinetics. Reduction rates of layered Mn oxides (birnessite and δ-MnO_2) under environmentally relevant conditions are within the regime observed for the transformation of δ-MnO_2 to todorokite by repeated redox cycling, which explains the abundance of todorokite (3 × 3 tunnel size) over other tunnel-structured Mn oxides with smaller tunnel sizes (e.g., 2 × 2 or 1 × 1 tunnel sizes) in natural environments.

common environmental reductants (e.g., organics, biotic species, and transition metals) and the redox rates of Mn observed in ocean sediments may be similar to or slower than that obtained from our 100 mV/s CV scans (Figure 6 and Table S7). Direct comparison of dissolved Mn^{2+}(aq) oxidation rates using pseudo-first-order reaction constants (k_{obs}) is limited because homogeneous oxidation rates in aqueous solution by biotic and photochemical processes cannot be normalized by surface area. However, reduction rates without surface area normalization are comparable to or faster than oxidation rates, suggesting that the rates for natural oxidation processes are likely to be similar to or slower than that obtained from our 100 mV/s CV scans (Figure S9). Thus, our findings suggest that the natural abundance of todorokite over other tunnel-structured Mn oxides is plausibly due to kinetics and electron flux limitations posed by natural oxidation and reduction processes. Using previously reported redox rates of Mn in ocean sediments[6] and assuming 300 times of redox cycles as used in this study, we were able to preliminarily estimate the time required for the transformation of δ-MnO_2 to todorokite in sediments. We used the redox rates between dissolved Mn^{2+}(aq) and Mn(III) in the pore water of ocean sediments[6] because there were no previous studies on the redox rates between structured Mn(II) and Mn(IV) in MnO_2 (diagenetic process) in natural systems. The estimated time for the transformation of δ-MnO_2 to todorokite ranges from ~0.1 to ~10 years with 300 redox cycles (Text S5 and Table S8). We note that the estimated time has a large range due to the limitation of available data, and the reaction time in natural systems may also vary significantly depending on environmental factors. Nonetheless, this study and the calculated estimation provides an initial step for future studies to explain the formation of todorokite and contribution of diagenesis processes on the diversity of Mn oxides in the presence of repeated redox cycles in nature.

■ CONCLUSION

Overall, our case study on the transformation of layer to tunnel structure in Mn oxides further emphasized the complex processes that can be involved in the formation of natural minerals. In this case, the occurrence of tunnel-structured natural Mn oxides may not always be due to single one-run

reactions but rather more likely due to repeated redox reactions and structural evolution cycles. In this study we used electrochemical methods to reasonably simulate and accelerate the reactions involving Mn oxides in nature. The results not only revealed the transformation mechanisms in great detail but also disclosed the significant role of kinetics and electron flux in the phase selection among different polymorphs of tunnel-structured Mn oxides, which explains the predominance of certain tunnel-structured Mn oxides in natural environments. The new insights revealed in this study may also provide new angles for interpreting the existence, evolution, and weathering of minerals and their relationships within the geological environments of planetary bodies such as the Earth and beyond.

■ ASSOCIATED CONTENT

ⓢ Supporting Information

The Supporting Information is available free of charge at https://pubs.acs.org/doi/10.1021/jacs.9b12266.

> Materials and Methods, XRD, HRTEM, XAS, electrochemical tests, structure of MnO_2, summary of redox rates, and thermodynamics and kinetics data in comparison with data surveyed from the literature (PDF)

■ AUTHOR INFORMATION

Corresponding Authors

Hailong Chen − *Georgia Institute of Technology, Atlanta, Georgia;* ⓘ orcid.org/0000-0001-8283-2860; Email: hailong.chen@me.gatech.edu

Yuanzhi Tang − *Georgia Institute of Technology, Atlanta, Georgia;* ⓘ orcid.org/0000-0002-7741-8646; Email: yuanzhi.tang@eas.gatech.edu

Other Authors

Haesung Jung − *Georgia Institute of Technology, Atlanta, Georgia*

Martial Taillefert − *Georgia Institute of Technology, Atlanta, Georgia;* ⓘ orcid.org/0000-0003-2053-6462

Jingying Sun − *University of Houston, Houston, Texas*

Qian Wang − *Georgia Institute of Technology, Atlanta, Georgia*

Olaf J. Borkiewicz − *Argonne National Laboratory, Argonne, Illinois*

Pan Liu − *Georgia Institute of Technology, Atlanta, Georgia*

Lufeng Yang − *Georgia Institute of Technology, Atlanta, Georgia*

Shuo Chen − *University of Houston, Houston, Texas*

Complete contact information is available at: https://pubs.acs.org/10.1021/jacs.9b12266

Notes

The authors declare no competing financial interest.

■ ACKNOWLEDGMENTS

■ REFERENCES

(1) Yano, J.; Yachandra, V. Mn_4Ca Cluster in Photosynthesis: Where and How Water is Oxidized to Dioxygen. *Chem. Rev.* **2014**, *114* (8), 4175−4205.

(2) Keiluweit, M.; Nico, P.; Harmon, M. E.; Mao, J.; Pett-Ridge, J.; Kleber, M. Long-term litter decomposition controlled by manganese redox cycling. *Proc. Natl. Acad. Sci. U. S. A.* **2015**, *112* (38), E5253−E5260.

(3) Butterfield, C. N.; Soldatova, A. V.; Lee, S.-W.; Spiro, T. G.; Tebo, B. M. Mn (II, III) oxidation and MnO_2 mineralization by an expressed bacterial multicopper oxidase. *Proc. Natl. Acad. Sci. U. S. A.* **2013**, *110* (29), 11731−11735.

(4) Lu, A.; Li, Y.; Ding, H.; Xu, X.; Li, Y.; Ren, G.; Liang, J.; Liu, Y.; Hong, H.; Chen, N.; Chu, S.; Liu, F.; Li, Y.; Wang, H.; Ding, C.; Wang, C.; Lai, Y.; Liu, J.; Dick, J.; Liu, K.; Hochella, M. F. Photoelectric conversion on Earth's surface via widespread Fe- and Mn-mineral coatings. *Proc. Natl. Acad. Sci. U. S. A.* **2019**, *116* (20), 9741−9746.

(5) Lovley, D. R.; Holmes, D. E.; Nevin, K. P. Dissimilatory Fe(III) and Mn(IV) reduction. *Adv. Microb. Physiol.* **2004**, *49*, 219−286.

(6) Madison, A. S.; Tebo, B. M.; Mucci, A.; Sundby, B.; Luther, G. W. Abundant porewater Mn (III) is a major component of the sedimentary redox system. *Science* **2013**, *341* (6148), 875−878.

(7) Nico, P. S.; Anastasio, C.; Zasoski, R. J. Rapid photo-oxidation of Mn (II) mediated by humic substances. *Geochim. Cosmochim. Acta* **2002**, *66* (23), 4047−4056.

(8) Jung, H.; Chadha, T.; Kim, D.; Biswas, P.; Jun, Y.-S. Photochemically-assisted Fast Abiotic Oxidation of Manganese and Formation of $δ−MnO_2$ Nanosheets in Nitrate Solution. *Chem. Commun.* **2017**, *53*, 4445−4448.

(9) Learman, D.; Voelker, B.; Vazquez-Rodriguez, A.; Hansel, C. Formation of manganese oxides by bacterially generated superoxide. *Nat. Geosci.* **2011**, *4* (2), 95−98.

(10) Spiro, T. G.; Bargar, J. R.; Sposito, G.; Tebo, B. M. Bacteriogenic manganese oxides. *Acc. Chem. Res.* **2010**, *43* (1), 2−9.

(11) Canfield, D. E.; Thamdrup, B.; Hansen, J. W. The anaerobic degradation of organic matter in Danish coastal sediments: iron reduction, manganese reduction, and sulfate reduction. *Geochim. Cosmochim. Acta* **1993**, *57* (16), 3867−3883.

(12) Trouwborst, R. E.; Clement, B. G.; Tebo, B. M.; Glazer, B. T.; Luther, G. W. Soluble Mn (III) in suboxic zones. *Science* **2006**, *313* (5795), 1955−1957.

(13) Post, J. E. Manganese oxide minerals: Crystal structures and economic and environmental significance. *Proc. Natl. Acad. Sci. U. S. A.* **1999**, *96* (7), 3447−3454.

(14) Huang, J.; Zhong, S.; Dai, Y.; Liu, C.-C.; Zhang, H. J. Effect of MnO_2 phase structure on the oxidative reactivity toward contaminant degradation. *Environ. Sci. Technol.* **2018**, *52*, 11309−11318.

(15) Remucal, C. K.; Ginder-Vogel, M. A critical review of the reactivity of manganese oxides with organic contaminants. *Environ. Sci. Process. Impact* **2014**, *16* (6), 1247−1266.

(16) Johnson, J. E.; Webb, S. M.; Thomas, K.; Ono, S.; Kirschvink, J. L.; Fischer, W. W. Manganese-oxidizing photosynthesis before the rise of cyanobacteria. *Proc. Natl. Acad. Sci. U. S. A.* **2013**, *110* (28), 11238−11243.

(17) Kurzweil, F.; Wille, M.; Gantert, N.; Beukes, N. J.; Schoenberg, R. Manganese oxide shuttling in pre-GOE oceans−evidence from molybdenum and iron isotopes. *Earth Planet. Sci. Lett.* **2016**, *452*, 69−78.

(18) Frei, R.; Gaucher, C.; Poulton, S. W.; Canfield, D. E. Fluctuations in Precambrian atmospheric oxygenation recorded by chromium isotopes. *Nature* **2009**, *461* (7261), 250−253.

(19) Planavsky, N. J.; Reinhard, C. T.; Wang, X.; Thomson, D.; McGoldrick, P.; Rainbird, R. H.; Johnson, T.; Fischer, W. W.; Lyons,

T. W. Low Mid-Proterozoic atmospheric oxygen levels and the delayed rise of animals. *Science* **2014**, *346* (6209), 635−638.

(20) Owens, J. D.; Nielsen, S. G.; Horner, T. J.; Ostrander, C. M.; Peterson, L. C. Thallium-isotopic compositions of euxinic sediments as a proxy for global manganese-oxide burial. *Geochim. Cosmochim. Acta* **2017**, *213*, 291−307.

(21) Romano, C. A.; Zhou, M.; Song, Y.; Wysocki, V. H.; Dohnalkova, A. C.; Kovarik, L.; Paša-Tolić, L.; Tebo, B. M. Biogenic manganese oxide nanoparticle formation by a multimeric multicopper oxidase Mnx. *Nat. Commun.* **2017**, *8*, 746−753.

(22) Li, Y.-F.; Zhu, S.-C.; Liu, Z.-P. Reaction network of layer-to-tunnel transition of MnO_2. *J. Am. Chem. Soc.* **2016**, *138* (16), 5371−5379.

(23) Xiao, Y.; Zhu, Y.-F.; Xiang, W.; Wu, Z.-G.; Li, Y.-C.; Lai, J.; Li, S.; Wang, E.; Yang, Z.-G.; Xu, C.-L.; Zhong, B.-H.; Guo, X.-D., Deciphering an Abnormal Layered-Tunnel Heterostructure Induced by Chemical Substitution for the Sodium Oxide Cathode. *Angew. Chem., Int. Ed.* **2019** DOI: 10.1002/anie.201912101.

(24) Yuan, Y.; He, K.; Byles, B. W.; Liu, C.; Amine, K.; Lu, J.; Pomerantseva, E.; Shahbazian-Yassar, R. Deciphering the Atomic Patterns Leading to MnO_2 Polymorphism. *Chem.* **2019**, *5* (7), 1793−1805.

(25) Yang, P.; Lee, S.; Post, J. E.; Xu, H.; Wang, Q.; Xu, W.; Zhu, M. Trivalent manganese on vacancies triggers rapid transformation of layered to tunneled manganese oxides (TMOs): Implications for occurrence of TMOs in low-temperature environment. *Geochim. Cosmochim. Acta* **2018**, *240*, 173−190.

(26) Chukhrov, F. V.; Gorshkov, A. I.; Sivtsov, A. V.; Beresovskaya, V. V. New data on natural todorokites. *Nature* **1979**, *278*, 631−632.

(27) Feng, X. H.; Zhu, M.; Ginder-Vogel, M.; Ni, C.; Parikh, S. J.; Sparks, D. L. Formation of nano-crystalline todorokite from biogenic Mn oxides. *Geochim. Cosmochim. Acta* **2010**, *74* (11), 3232−3245.

(28) Zhao, H.; Liang, X.; Yin, H.; Liu, F.; Tan, W.; Qiu, G.; Feng, X. Formation of todorokite from "c-disordered" H^+-birnessites: the roles of average manganese oxidation state and interlayer cations. *Geochem. Trans.* **2015**, *16* (1), 8.

(29) Bricker, O. Some stability relations in system Mn-O_2-H_2O at 25 degrees and 1 atm total pressure. *Am. Mineral.* **1965**, *50* (9), 1296−1354.

(30) Chen, B.-R.; Sun, W.; Kitchaev, D. A.; Mangum, J. S.; Thampy, V.; Garten, L. M.; Ginley, D. S.; Gorman, B. P.; Stone, K. H.; Ceder, G.; Toney, M. F.; Schelhas, L. T. Understanding crystallization pathways leading to manganese oxide polymorph formation. *Nat. Commun.* **2018**, *9* (1), 2553−2561.

(31) Borch, T.; Kretzschmar, R.; Kappler, A.; Cappellen, P. V.; Ginder-Vogel, M.; Voegelin, A.; Campbell, K. Biogeochemical redox processes and their impact on contaminant dynamics. *Environ. Sci. Technol.* **2010**, *44* (1), 15−23.

(32) Zhao, S.; Wang, Q.; Sun, J.; Borkiewicz, O. J.; Huang, R.; Saad, E. M.; Fields, B.; Chen, S.; Zhu, M.; Tang, Y. Effect of Zn coprecipitation on the structure of layered Mn oxides. *Chem. Geol.* **2018**, *493* (20), 234−245.

(33) Webb, S.; Fuller, C.; Tebo, B.; Bargar, J. Determination of uranyl incorporation into biogenic manganese oxides using X-ray absorption spectroscopy and scattering. *Environ. Sci. Technol.* **2006**, *40* (3), 771−777.

(34) Golden, D.; Chen, C.; Dixon, J. Synthesis of todorokite. *Science* **1986**, *231* (4739), 717−719.

(35) Bodeï, S.; Manceau, A.; Geoffroy, N.; Baronnet, A.; Buatier, M. Formation of todorokite from vernadite in Ni-rich hemipelagic sediments. *Geochim. Cosmochim. Acta* **2007**, *71* (23), 5698−5716.

(36) Yuan, Y.; Liu, C.; Byles, B. W.; Yao, W.; Song, B.; Cheng, M.; Huang, Z.; Amine, K.; Pomerantseva, E.; Shahbazian-Yassar, R.; Lu, J. Ordering Heterogeneity of [MnO_6] Octahedra in Tunnel-Structured MnO_2 and Its Influence on Ion Storage. *Joule* **2019**, *3* (2), 471−484.

(37) McKeown, D. A.; Post, J. E. Characterization of manganese oxide mineralogy in rock varnish and dendrites using X-ray absorption spectroscopy. *Am. Mineral.* **2001**, *86* (5−6), 701−713.

(38) Saratovsky, I.; Gurr, S. J.; Hayward, M. A. The structure of manganese oxide formed by the fungus Acremonium sp. strain KR21−2. *Geochim. Cosmochim. Acta* **2009**, *73* (11), 3291−3300.

(39) Santelli, C. M.; Webb, S. M.; Dohnalkova, A. C.; Hansel, C. M. Diversity of Mn oxides produced by Mn (II)-oxidizing fungi. *Geochim. Cosmochim. Acta* **2011**, *75* (10), 2762−2776.

(40) Grangeon, S.; Lanson, B.; Miyata, N.; Tani, Y.; Manceau, A. Structure of nanocrystalline phyllomanganates produced by fresh-water fungi. *Am. Mineral.* **2010**, *95* (11−12), 1608−1616.

(41) Larabi-Gruet, N.; Peulon, S.; Lacroix, A.; Chausse, A. Studies of electrodeposition from Mn (II) species of thin layers of birnessite onto transparent semiconductor. *Electrochim. Acta* **2008**, *53* (24), 7281−7287.

(42) Jung, H.; Chadha, T. S.; Min, Y.; Biswas, P.; Jun, Y.-S. Photochemically-assisted Synthesis of Birnessite Nanosheets and Their Structural Alteration in the Presence of Pyrophosphate. *ACS Sustainable Chem. Eng.* **2017**, *5* (11), 10624−10632.

(43) Lanson, B.; Drits, V. A.; Silvester, E.; Manceau, A. Structure of H-exchanged hexagonal birnessite and its mechanism of formation from Na-rich monoclinic buserite at low pH. *Am. Mineral.* **2000**, *85* (5−6), 826−838.